Vertical Engineering for Large Brillouin Gain in Unreleased Silicon-Based Waveguides

L. Mercadé, A.V. Korovin, Yan Pennec, J. Ahopelto, Bahram Djafari-Rouhani, A. Martínez

Vertical Engineering for Large Brillouin Gain in Unreleased Silicon-Based Waveguides

Laura Mercadé,[1] Alexander V. Korovin,[2,3] Yan Pennec,[3] Jouni Ahopelto,[4] Bahram Djafari-Rouhani,[3] and Alejandro Martínez[1,*]

[1] *Nanophotonics Technology Center, Universitat Politècnica de València, Camino de Vera s/n, Valencia 46022, Spain*

[2] *Institute for Physics of Semiconductors, NAS of Ukraine, Prospect Nauki, 41, Kiev 03028, Ukraine*

[3] *Institut d'Électronique, de Microélectronique et de Nanotechnologie, UMR CNRS 8520, Université de Lille, Cité Scientifique, Villeneuve d'Ascq 59655, France*

[4] *VTT Technical Research Centre of Finland Ltd, P.O. Box 1000, Espoo FI-02044 VTT, Finland*

(Received 4 November 2020; revised 19 January 2021; accepted 12 February 2021; published 8 March 2021)

Strong acousto-optic interaction in high-index waveguides and cavities generally requires the releasing of the high-index core to avoid mechanical leakage into the underlying low-index substrate. This complicates fabrication, limits thermalization, reduces the mechanical robustness, and hinders large-area optomechanical devices on a single chip. Here, we overcome this limitation by employing vertical photonic-phononic engineering to drastically reduce mechanical leakage into the cladding by adding a pedestal with specific properties between the core and the cladding. We apply this concept to a silicon-based platform, due to the remarkable properties of silicon to enhance optomechanical interactions and the technological relevance of silicon devices in multiple applications. Specifically, the insertion of a thick silicon nitride layer between the silicon guiding core and the silica substrate contributes to reducing gigahertz-frequency phonon leakage while enabling large values of the Brillouin gain in an unreleased platform. We numerically obtain values of the Brillouin gain around 300 $(\mathrm{W\,m})^{-1}$ for different configurations, which could be further increased by operation at cryogenic temperatures. These values should enable Brillouin-related phenomena in centimeter-scale waveguides or in more compact ring resonators. Our findings could pave the way toward large-area unreleased-cavity and waveguide optomechanics on silicon and other high-index photonic technologies.

DOI: 10.1103/PhysRevApplied.15.034021

I. INTRODUCTION

Stimulated Brillouin scattering (SBS) is a nonlinear process arising from photon-phonon interaction in material systems supporting both optical and acoustic propagating waves [1,2]. For many years, optical fibers have been the most extended platform to observe SBS and related phenomena [3]. Indeed, many applications—mainly in the context of microwave photonics [4]—have been developed, spanning from tunable microwave filters [5] to optical pulse storage [6]. The current trend toward miniaturization and on-chip integration of optical devices has also been followed in SBS-related phenomena and applications [7]. Initial demonstrations of on-chip SBS made use of a chalcogenide glass (Al_2S_3) as the guiding core material for both light and sound [8]. As in optical fibers, acousto-optic (AO) interaction via electrostriction and photoelasticity in the waveguide core is mainly responsible for the SBS [9]. Despite the fact that this approach enables large Brillouin gain and multiple SBS-based on-chip functionalities [10,11], it is not compatible with CMOS technology, which prevents massive integration with mainstream silicon photonic and electronic components.

Silicon was originally disregarded as an appropriate material for integrated SBS, since when placed over silica—as in standard silicon-on-insulator wafers—it cannot confine mechanical waves, which prevents strong AO coupling [12]. SBS in silicon waveguides requires the waveguide to be at least partly released so that phonon pathways toward the silica substrate are strongly inhibited [13–15]. Notably, the strong field confinement in a high-index wavelength-size silicon core not only results in enhanced AO volumetric interaction due to the large photoelastic effect in silicon but, in addition, the photon-phonon interaction is mediated by the radiation pressure exerted by the optical field on the interfaces, which scales up with the electric permittivity contrast at the boundary [9,16]. This

*amartinez@ntc.upv.es

has led to experiments reporting values of the Brillouin gain (G_B) well above 10^3 1/W m [14,15], which confirms the appropriateness of silicon as a material for integrated SBS. However, besides some recent exciting demonstrations, such as the case of a silicon Brillouin laser [17], the need for partial release of the silicon core complicates the fabrication (as it requires HF baths), reduces thermal dissipation, prevents the introduction of more sophisticated AO elements (required for building chip-scale data processors based on SBS [7]), and reduces the mechanical robustness of the device. Therefore, a silicon-compatible platform displaying mechanical robustness, large Brillouin gain, and low propagation losses while simultaneously not requiring the release of the silicon core is still lacking [7].

Recently, an approach for unreleased-silicon SBS based on a geometric softening technique has been proposed [18]. Here, two high-aspect-ratio silicon waveguides placed on a silica substrate and spaced by a thin slot have been shown to provide large G_B values for both backward and forward configurations. However, fabrication of this slotted structure becomes complicated because of the thin slot and optical propagation losses may become quite large because of the large area of the sidewall boundaries, so SBS has not been demonstrated in this system. Silicon nitride waveguides have also been shown to be good candidates for unreleased SBS-based devices, mainly because they show extremely low linear losses and negligible two-photon absorption [19]. In this case, phonons are not confined in the waveguide core, which results in G_B values that are orders of magnitude smaller than in released silicon waveguides [20] and, consequently, a high operating optical power and ultralong waveguides are required.

In this work, we introduce an unreleased silicon-based waveguide that can be lithographically defined to confine both optical and mechanical waves in the silicon core and provide large G_B values. We engineer the waveguide vertically by inserting a thick silicon nitride layer between the top silicon waveguide and the silica substrate. This reduces phonon leakage enormously and enables strong localization of the mechanical field in the silicon core, which leads to ($G_B \simeq 300$ 1/W m) in both forward- and backward-stimulated Brillouin scattering processes at room temperature. Moreover, G_B can be enhanced up to 10^5 1/W m at low temperature as a result of larger mechanical Q factors. From the fabrication point of view, the whole structure could be fabricated using standard fabrication processes, such as chemical-vapor deposition, lithography (either electronic or optical), and etching, not requiring either partial or full releasing via HF baths.

II. DESCRIPTION OF THE PHOTONIC-PHONONIC WAVEGUIDING SYSTEM

The key idea of our AO waveguiding system is to place, between the high-index guiding core (silicon) and the low-index substrate (silica), an intermediate layer made of a material having both a refractive index lower than that of silicon (to ensure photon confinement in the silicon layer) and a sound speed higher than that of silicon (to avoid phonon leakage from silicon to silica). We choose silicon nitride (Si_3N_4) to build this intermediate layer, which is completely compatible with silicon photonics technology. Notably, even though it depends on its state (crystalline or amorphous) as well as the deposition method, both the speed of sound and stiffness are higher in Si_3N_4 than in silicon [20–22], which is a basic requirement for the reduction of mechanical leakage from the silicon core to the silica substrate.

Figure 1(a) shows a transverse cross section of the proposed waveguiding system: a silicon (Si) core (width w, thickness b) lies upon a Si_3N_4 layer (width w, total

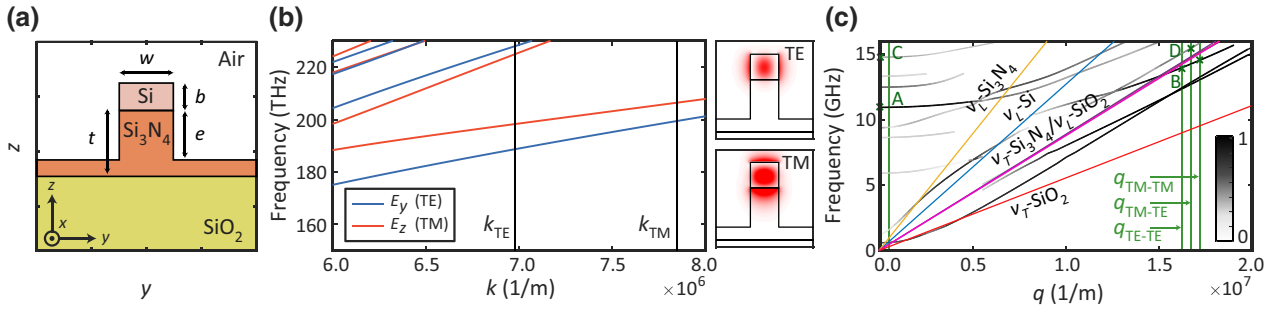

FIG. 1. The Si-Si_3N_4 photonic-phononic waveguide. (a) The material cross section of the waveguiding structure. (b) The calculated dispersion relation of the TE-like and TM-like optical guided modes with the optical wave vectors involved for each mode. The insets show the computed E_y and E_z components of the optical TE-like and TM-like waveguide modes, respectively. (c) The calculated dispersion relation for the mechanical modes. The interfaces between Si/Si_3N_4 and air are treated as free boundaries and perfectly matched layer conditions are imposed at the substrate-limit interfaces. Here, the color scale shows the acoustic localization factor of the mechanical mode within the silicon core (this factor is 1 for a mechanical mode completely confined in the silicon core). The optical and mechanical wave vectors involved in some of the calculations in the text are also depicted in (b) and (c), respectively. The dimensions of the waveguide in (b) and (c) are $w = 325$ nm, $b = 0.9w$, $e = 450$ nm, and $t = 600$ nm.

thickness t, etched thickness e) that is placed over a silica substrate, which we assume to be semi-infinite. For the numerical simulations, we consider that the refractive indices of the involved materials at telecom wavelengths are $n_{\mathrm{Si}} = 3.48$, $n_{\mathrm{SiO_2}} = 1.44$, and $n_{\mathrm{Si_3N_4}} = 2$. By choosing the dimensions properly, the waveguiding system can support a set of optical guided modes (namely, the TE-like and TM-like modes) in the relevant telecom band, as depicted in Fig. 1(b). To perform mechanical simulations, we choose the following parameters. The photoelastic constants in contracted notation are $[p_{11} = -0.09, p_{12} = 0.017, p_{44} = -0.051]$ for silicon [23], which is also assumed to be an anisotropic material with a density $\rho = 2329$ (kg/m^3) and stiffness constants in Voigt notation of $[c_{11} = 2.17 \times 10^{11}$, $c_{12} = 4.83 \times 10^{10}$, $c_{44} = 6.71 \times 10^{10}]$ (Pa) [24,25]. For the silica substrate, we consider $[p_{11} = 0.121, p_{12} = 0.27, p_{44} = -0.075]$ as photoelastic constants [26] while to define the mechanical properties we use a Young's modulus of 73.1 (Pa), a Poisson's ratio of $\nu = 0.17$, and a density $\rho = 2203$ (kg/m^3). Finally, Si_3N_4 is also considered to be an anisotropic material with $\rho = 3100$ (kg/m^3) and stiffness constants of $[c_{11} = 4.33 \times 10^{11}, c_{33} = 5.74 \times 10^{11}, c_{44} = 5.74 \times 10^{11}$, $c_{66} = 1.19 \times 10^{11}$, $c_{12} = 1.95 \times 10^{11}$, $c_{13} = 1.25 \times 10^{11}]$ (Pa) [27]. Note that the photoelastic coefficients of the Si_3N_4 are assumed to be equal to those of silica, as they are largely unknown in the literature [28], though a recent experiment has reported an experimental value $p_{12} = 0.047$ [20]. With these mechanical parameters and the previous dimensions of the waveguide, we obtain a set of mechanical modes as shown in Fig. 1(c), where q is the wave vector along the axis of the waveguide. More details of the mechanical simulations, including the effect of the area of the substrate considered in the calculations, can be found in the Supplemental Material [29].

Note that the mechanical dispersion relation shows all the modes that we can find in the structure and the color scale represents the acoustic localization factor in the silicon core, calculated as $(\int_{S_1} dS|\mathbf{u}|^2)/(\int_{S_2} dS|\mathbf{u}|^2)$, where u is the total mechanical mode displacement and $S1$ and $S2$ denote the silicon core and the full cross section under consideration, respectively. The darker lines represent a localization close to unity, which means that the mechanical mode is well located in the silicon region. In contrast, the lighter lines show less localized modes. In Fig. 1(c), the mechanical modes with the highest Brillouin gain (see below) for different intramodal and intermodal configurations are highlighted. The mechanical modes termed A and C give the highest G_B values in the case of forward intramodal TE and TM coupling, respectively. The mechanical mode B is involved in both backward intramodal TE-TE and TM-TM interactions, while the mechanical mode D is the one that gives a higher G_B value in backward intermodal TE-TM SBS.

III. AO INTERACTION AND BRILLOUIN GAIN

Propagating optical and mechanical modes interact via volumetric and surface processes as long as energy and momentum are conserved [7,9,12]. In an AO waveguiding system such as the one presented here, G_B for a certain mechanical mode can be obtained as follows [23]:

$$G_B = \frac{2\omega Q_m}{\Omega_m^2} \frac{|\langle \mathbf{f}, \mathbf{u}_m \rangle|^2}{\langle P_p \rangle \langle P_s \rangle \langle \mathbf{u}_m, \rho \mathbf{u}_m \rangle}, \tag{1}$$

where m is the mechanical mode number (omitted in what follows for the sake of simplicity), $\langle u_m, \rho u_m \rangle$ is the mechanical mode effective mass, $\langle P \rangle = \frac{1}{2} v_g \langle \mathbf{E}, \epsilon \mathbf{E} \rangle$ is the averaged Poynting vector for guided pump ("p") and Stokes ("s") waves, $\mathbf{E} = (\mathbf{E}_p e^{i(-k_p x + \omega_p t)} + \mathbf{E}_s e^{i(-k_s x + \omega_s t)})/2 + c.c.$ is the electric field, $\mathbf{D} = \epsilon \mathbf{E}$ is the displacement field, ϵ is the material permittivity, v_g is the group velocity, $\mathbf{f}$ is the optical force, $\mathbf{u} = u_x \mathbf{x} + u_y \mathbf{y} + u_z \mathbf{z}$ is the elastic displacement caused by the total optical power created by the pump and Stokes waves, and Ω_m and Q_m are the frequency and the mechanical quality factor of the involved mechanical mode at $q = k_p - k_s$.

Note that in the calculations performed in Secs. IV and V, we assume a mechanical Q factor $Q_m = 10^3$, meaning that the mechanical damping is limited by material losses [30]. This is a typical convention followed in cavity and waveguide optomechanics at gigahertz frequencies when operated at room temperature. However, in our calculations below, we retain the original mechanical quality factor for modes showing $Q_m < 10^3$ in simulations, in order to not overestimate leaky modes. In Sec. VI, we include a discussion on the situation when operating at cryogenic temperatures where much higher mechanical Q factors can be expected.

As a result of the continuous translational symmetry along the propagation axis, the overlap between the optical and mechanical fields in Eq. (1) is defined by the inner product between two vector fields with integration over the whole waveguide cross section, S:

$$\langle \mathbf{A}, \mathbf{B} \rangle = \int_S dS(\mathbf{A} \cdot \mathbf{B}^*). \tag{2}$$

We consider the total optical force $\mathbf{f}$ exerted by pump and Stokes waves and originating from electrostriction bulk and interface forces as well as radiative pressure [23]. The elastodynamics equation, including the electrostrictive stress induced by the optical field, reads as follows [31]:

$$\rho \frac{\partial^2 u_i}{\partial t^2} - [c_{ijkl} u_{k,l}]_j = -\sigma_{ij,j}^{es}, \tag{3}$$

where c_{ijkl} is the rank-4 tensor of elastic constants, $\sigma_{ij}^{es} = -\frac{1}{2}\epsilon_0 \chi_{klij} E_k E_l$ is the electrostrictive stress tensor, with

the rank-4 susceptibility tensor $\chi_{klij} = \epsilon_{km}\epsilon_{ln}p_{mnij}$ ($\sigma_{ij}^{es} = -\frac{1}{2}\epsilon_0\epsilon_{km}\epsilon_{ln}p_{mnij}E_kE_l$), p_{mnij} is the photoelastic tensor, and ϵ_0 is the permittivity of vacuum.

Finally, the overlap between the optical and mechanical fields in Eq. (1) is defined as

$$\langle \mathbf{f}, \mathbf{u} \rangle = \iint_S dS(\mathbf{f}^{\mathrm{ES}} \cdot \mathbf{u}^*) + \oint_{\partial S} dl(\mathbf{F}^{\mathrm{ES}} \cdot \mathbf{u}^*) + \oint_{\partial S} dl(\mathbf{F}^{\mathrm{RP}} \cdot \mathbf{u}^*), \tag{4}$$

where $f^{\mathrm{ES}} = -\nabla\widehat{\sigma}$ is the electrostriction (bulk) force, $\mathbf{F}^{\mathrm{ES}} = (\widehat{\sigma}^{(1)} - \widehat{\sigma}^{(2)}) \cdot \mathbf{n}$ is the electrostriction interface force, and $\mathbf{F}^{\mathrm{RP}} = (\widehat{T}^{(1)} - \widehat{T}^{(2)}) \cdot \mathbf{n}$ is the radiative pressure, $\mathbf{n}$ being the normal to the boundary between contacting media. Here, the index (1) describes the internal medium and (2) describes the outward medium of the interface. The radiative pressure is defined by the Maxwell stress tensor, $T_{ij} = \varepsilon_0\varepsilon(E_iE_j - \frac{1}{2}\delta_{ij}E^2)$, and can be reduced to the expression

$$\mathbf{F}^{\mathrm{RP}} = \frac{1}{2}[\varepsilon_0(\varepsilon_1 - \varepsilon_2)E_{pt}E_{st}^* - \varepsilon_0^{-1}(\varepsilon_1^{-1} - \varepsilon_2^{-1})D_{pn}D_{sn}^*] \cdot \mathbf{n}. \tag{5}$$

IV. FORWARD-STIMULATED BRILLOUIN SCATTERING

In the case of released silicon waveguides, mechanical modes are completely guided even when $q = 0$ because phonons cannot escape from the silicon core. Therefore, large values of G_B in forward-stimulated Brillouin scattering (FSBS) processes are obtained by simulations [23] and confirmed experimentally [14]. When the silicon—or Si_3N_4—core is on top of a silica substrate, there is no way to confine the phonons in that location since the sound velocity in silica substrate is lower than in the core. In our system, even though the mechanical modes at $q \approx 0$ (required for FSBS) are leaky (or, in other words, ideally they do not have an infinite mechanical Q factor), they can still be largely confined inside the silicon core, as shown in Fig. 1(c) (see also the results below). This is because the intermediate Si_3N_4 layer partially prevents the leakage of phonons into the silica substrate. Therefore, we perform numerical calculations to evaluate G_B for the FSBS process in two situations: intramodal interaction between either TE or TM optical modes.

The results for intramodal TE FSBS are summarized in Fig. 2. Here, we can observe the profiles of the optical forces obtained from bulk and interface electrostrictive (red) and radiation (blue) pressure effects [Fig. 2(a)]. For these force profiles, the mechanical mode termed A in Fig. 1(c) gives the highest gain. The displacement of this mechanical mode, which has an acoustic localization factor of 0.989 and a theoretical Q factor—that is, neglecting material losses—of 2×10^5, is depicted in Fig. 2(b), where it can be appreciated that the displacement field is mainly located at the top interface of the silicon core. The strong localization in the silicon core is confirmed by calculating the accumulated mechanical displacement, obtained as $u_{\mathrm{int}} = \int_{-w/2}^{w/2} |u|^2 dy$, and the maximum displacement as a function of the height, as depicted in Fig. 2(c). This leads to relatively large G_B values ($G_{B,\mathrm{TE}} \approx 300$ 1/W m) for the mechanical mode A as long as the etching e is deeper than 250 nm [Fig. 2(d)]. Indeed, the general trend is that the Brillouin gain grows with e and finally saturates when there is full etching of the silicon nitride layer ($e = t$). When calculating the Brillouin gain as a function of w, we can see that there is a waveguide width that maximizes the gain, as shown in Fig. 2(e). Importantly, changing the waveguide width also allows us to tune the mechanical frequency f_m. As shown in Fig. 2(e), changing the waveguide width from 290 to 450 nm tunes f_m between approximately 8 GHz and approximately 12 GHz. This is an important feature because it may allow us to tune the Brillouin frequency across the whole X band, which is very important

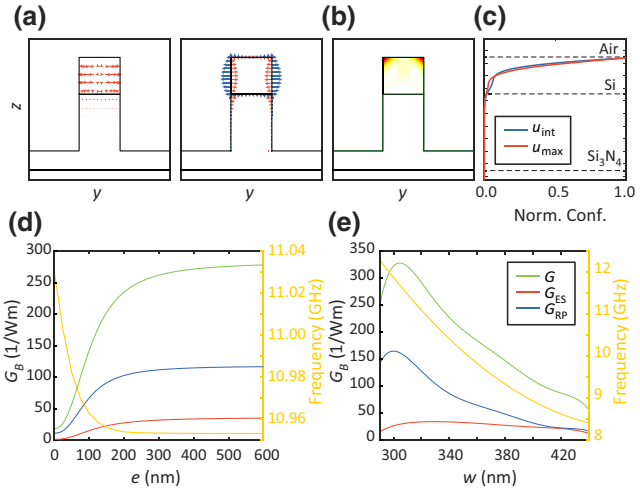

FIG. 2. The intramodal TE FSBS interaction at $q = 0$. (a) The optical-force distributions arising from the interaction of two copropagating TE-like modes (Stokes and pump waves). The left panel shows the bulk electrostrictive force (red) and the right panel shows the electrostrictive (red) and radiation-pressure (blue) interface forces. (b) The total displacement of the mechanical mode with the highest G_B [termed A in Fig. 1(c)]. (c) The normalized confinement distribution of the total accumulated displacement (blue) and the maximum displacement (red). (d) The total Brillouin gain G_B (green) and its electrostrictive (red) and radiation-pressure (blue) contributions as a function of the etching depth e of the Si_3N_4 layer for a structure with dimensions $w = 325$ nm, $b = 0.9w$, and $t = 600$ nm. (e) The total Brillouin gain G_B (green) and its electrostrictive (red) and radiation-pressure (blue) contributions as a function of the waveguide width w for $e = 450$ nm and $t = 600$ nm. In (d) and (e), the mechanical frequency is depicted in yellow.

in many microwave applications. As the mechanical mode is mainly confined on the edges of the upper surface of the silicon region, as can be appreciated in Fig. 2(b), the main contribution to the total Brillouin gain is given by the radiation-pressure force at that interface. Regarding the electrostrictive contribution, it has to be noted that the field profiles of the bulk and interface contributions have opposite directions, resulting in a destructive interference of the total contribution. Nevertheless, the radiation pressure and the total electrostrictive contributions interfere constructively for this configuration, leading to the relatively large calculated values of the Brillouin gain.

The results for intramodal TM FSBS are summarized in Fig. 3. Again, we obtain relatively large values of G_B [Fig. 3(d)], peaking close to 300 1/W m. As in the previous case, we also observe that changing the waveguide width w allows us to tune the mechanical frequency and optimize the AO coupling. Indeed, the best configuration can be found for $e \approx 400$ nm and $w \approx 360$ nm, with a mechanical frequency $f_m \approx 13$ GHz. Here, the main contribution to the total gain comes from the electrostrictive effect, for

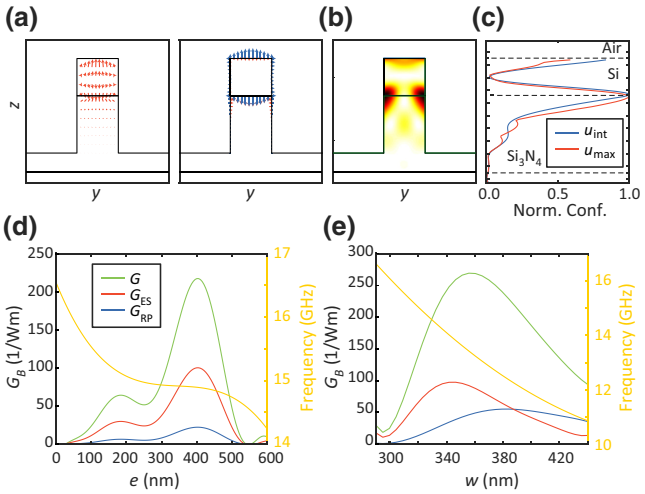

FIG. 3. The intramodal TM FSBS interaction at $q = 0$. (a) The optical-force distributions arising from the interaction of two copropagating TM-like modes (Stokes and pump waves) for FSBS. The left panel shows (in red) the bulk electrostrictive force and the right panel shows the electrostrictive (red) and radiation-pressure (blue) interface forces. (b) The calculated displacement of the mechanical mode with the highest G_B [termed C in Fig. 1(c)]. (c) The normalized distribution of the total accumulated displacement (blue) and maximum displacement (red) as a function of the height of the structure. (d) The total G_B gain (green) and its electrostrictive (red) and radiation-pressure (blue) contributions as a function of the etching depth of the Si_3N_4 layer for a structure with dimensions $w = 325$ nm, $b = 0.9w$, and $t = 600$ nm. (e) The total G_B (green) and its electrostrictive (red) and radiation-pressure (blue) contributions as a function of the waveguide width w for $e = 450$ nm and $t = 600$ nm. In (d) and (e), the mechanical frequency is depicted in yellow.

which the bulk and interface field profiles now have the same direction in the region where the mode is localized. The main difference with respect to the TE case is that the mechanical mode that couples with the force distributions [Fig. 3(b)] in this configuration is not so well confined in the silicon core as before. This relatively poor confinement can also be observed in Fig. 3(c), where it is seen that part of the mechanical displacement is in the pedestal region, as well as from the calculation of the acoustic localization factor, which is now approximately 0.5, and the calculated mechanical quality factor, which is 10^2. In this case, as the calculated Q_m is lower than 10^3, the upper limit due to material losses at room temperature, we use $Q_m = 10^2$ in the calculations of the Brillouin gain.

V. BACKWARD-STIMULATED BRILLOUIN SCATTERING

The process of backward-stimulated Brillouin scattering (BSBS) involves large-q mechanical modes that should ideally be placed below the sound line of the silica substrate in order to completely suppress mechanical leakage. Additionally, mechanical modes over the sound line could be well confined in the silicon core and give rise to strong AO interaction and a large Brillouin gain, as above in the case of FSBS. In our study, we first consider intramodal BSBS resulting from the interaction of two counterpropagating TE-like optical modes and again select the mechanical mode providing a larger G_B [in the case, the mode B in Fig. 1(c)]. We obtain $G_B \approx 340$ 1/W m at frequencies $f_m \approx 12.4$ GHz for the dimensions specified in Fig. 4(d). In this configuration, the electrostrictive contribution in the total gain is nearly zero. This results from the destructive interference between both the bulk and the interface forces that, as seen in Fig. 4(b), are opposing. Besides that, we obtain a mechanical mode that is highly localized in the silicon core [Figs. 4(b) and 4(c)]. In this case, the calculated mechanical quality factor is 2.8×10^7, much larger than in the forward configuration. This could be explained as being due to the fact that, unlike the modes at $q \approx 0$, this mechanical mode is placed below the longitudinal speed of sound in silica, as observed in Fig. 1(c). Regarding the acoustic localization factor, we obtain a value of 0.9993, in accordance with a high localized mechanical mode.

In the case of the backward intramodal TM configuration (Fig. 5), we observe that unlike in the intramodal TE BSBS case, the electrostriction contribution gain now reaches values around 600 1/W m. However, the radiation-pressure and electrostriction contributions interfere destructively, thus resulting in $G_B \approx 220$ 1/W m for the mode termed B in Fig. 1(c) [see the displacement profile in Fig. 5(b)]. Nevertheless, as the mechanical mode has a large acoustic localization factor (0.9995) as well as an ultrahigh mechanical quality factor ($Q_m = 2.3 \times 10^7$) there is a slight improvement in the total gain when

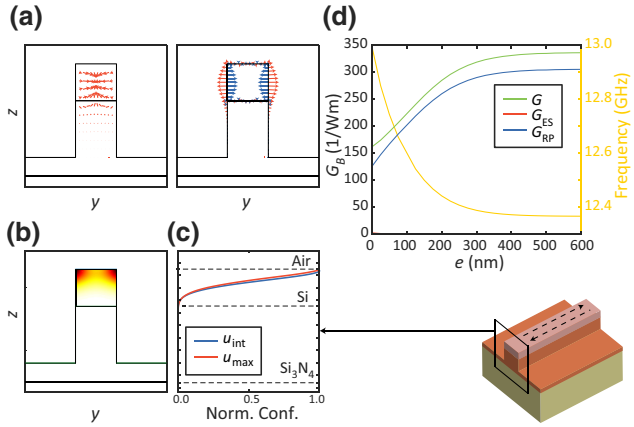

FIG. 4. The intramodal TE BSBS interaction at $q = 2k_{TE}$. (a) The optical-force distributions arisen from the interaction of two counterpropagating TE-like modes. The left panel shows the bulk electrostrictive force while the right panel shows the electrostrictive (red) and radiation-pressure (blue) interface forces. (b) The total mechanical displacement of the mode with the highest G_B [termed B in Fig. 1(c)]. (c) The normalized distribution of the total accumulated displacement (blue) and the maximum displacement (red). (d) The total Brillouin gain (green) and its electrostrictive (red) and radiation-pressure (blue) contributions as a function of e for waveguide dimensions $w = 325$ nm, $b = 0.9w$, and $t = 600$ nm. In (d), the mechanical frequency is depicted in yellow.

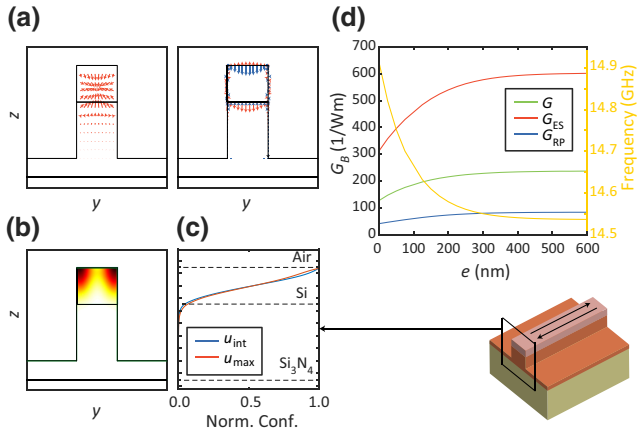

FIG. 5. The intramodal TM BSBS interaction at $q = 2k_{TM}$. (a) The optical-force distributions arising from the interaction of two counterpropagating TM-like modes. The left panel shows the bulk electrostrictive force (red) and the right panel shows both the electrostrictive (red) and radiation-pressure (blue) interface forces. (b) The total mechanical displacement of the mode with the highest gain [termed B in Fig. 1(c)]. (c) The normalized distribution of the total accumulated displacement (blue) and the maximum displacement (red). (d) The Brillouin gain (green) and its electrostrictive (red) and radiation-pressure (blue) contributions as a function of e for $w = 325$ nm, $b = 0.9w$, and $t = 600$ nm. The mechanical frequency is depicted in yellow.

the etching depth increases. Still, these values could be sufficient for practical applications.

We also calculate the Brillouin gain for the intermodal TE-TM interaction. Even though the results are not shown here for the sake of simplicity, the calculated values are lower than in the case of intramodal interactions. This is probably due to the fact that the mode that gives the highest gain for this configuration at $q = k_{TM} - k_{TE}$ is the mode termed D in Fig. 1(c), which has a localization that is poorer than for the other mechanical modes even at high wave vectors. Still, further design of the waveguide may result in large G_B values for intermodal interaction.

VI. ENHANCEMENT OF THE BRILLOUIN GAIN AT LOW TEMPERATURE

As we note in previous sections, the mechanical Q factor is assumed to be $Q_m = 10^3$ because the mechanical damping is limited by the material loss at room temperature. However, this is not the case if we work at low temperatures, where the Q_m factor can be enhanced up to much higher values [30]. If we study the evolution of the ideal mechanical quality factor (that is, as obtained from the simulations and neglecting material losses) of the mechanical modes involved in our configurations, we can see that it grows as the etching of the Si_3N_4 layer e is increased up to its maximum (which is the maximum thickness of the silicon nitride layer, $t = 600$ nm). This effect is clearly seen in Fig. 6(a) for the case of the intramodal TE FSBS interaction. Here, we can also see the evolution of the acoustic localization factor (in yellow) in the silicon core as a function of e. It can be appreciated that the mechanical mode is almost totally confined (the localization factor is almost 1) regardless of the etching depth e and it is only reduced in the case in which there is no pedestal and the silicon waveguide lies on a Si_3N_4 substrate. The modified low-temperature Brillouin gain, taking into account the ideal Q_m and introducing it in Eq. (1), is shown in Fig. 6(b). This means that for the same situation as the one described in Fig. 2(d), the total Brillouin gain is increased from 300 1/W m up to 1.5×10^5 1/W m, which should be attainable when operating at cryogenic temperatures.

VII. PRACTICAL IMPLEMENTATION

Although the focus is on the theoretical treatment of unreleased silicon waveguides, here we introduce a potential route for implementation of the optomechanical system that we propose. The AO performance of the waveguiding structure under study and, in particular, its ability to confine mechanical waves in the silicon core, depend on the mechanical behavior of the intermediate layer. In our calculations, we model the Si_3N_4 layer assuming that it is crystalline and using the parameters reported in Ref. [27]. The mechanical properties of stoichiometric Si_3N_4 depend only slightly on the crystal lattice orientation [32] and on

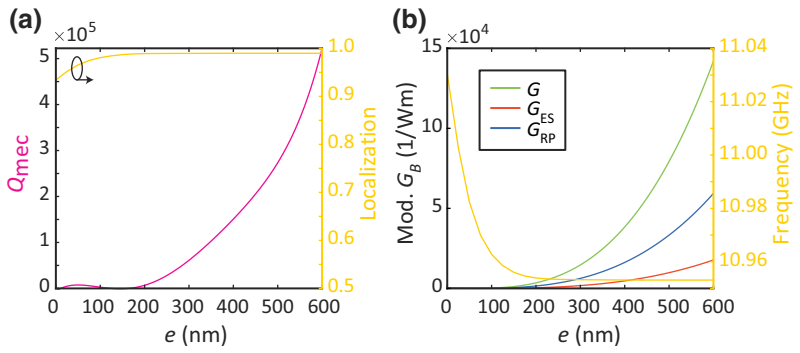

FIG. 6. The intramodal TE FSBS interaction at $q = 0$ at low temperature (assuming that mechanical damping is not limited by material losses). (a) Q_m (purple) and the acoustic localization factor (yellow) as a function of e. (b) The Brillouin gain as a function of e for $w = 325$ nm, $b = 0.9w$, and $t = 600$ nm calculated using the ideal Q_m factor in (a).

whether the material is single crystalline or polycrystalline. A straightforward route for fabrication is to use single-crystalline Si_3N_4 substrates with an epitaxial nitride layer, on top of which a thin layer of silicon is deposited and patterned to form the waveguides. The drawback here is the very high cost of the substrates and the limited integrability with the standard silicon technology. Low-pressure chemical-vapor deposition (LPCVD) is a common method for the deposition of Si_3N_4 films on silicon or silicon dioxide. The challenge with LPCVD is the very high tensile stress built into stoichiometric nitride films. The solution is to grow silicon-rich low-stress silicon nitride (SiN_x) and the most plausible method for fabrication is to follow the design shown in Fig. 1, with a thick thermal oxide on a silicon substrate and replacement of the stoichiometric Si_3N_4 by SiN_x. The tensile stress of SiN_x is of the order of a few hundreds of MPa, which can be matched with the tensile stress of nanocrystalline silicon, forming the waveguide. The tensile stress of nanocrystalline silicon can be tuned from a few tens of MPa to a few hundreds of MPa by thermal treatment [33,34]. Furthermore, nanocrystalline silicon has optical and mechanical properties that are very similar to those of crystalline silicon, making it suitable for the waveguides. The excess of Si in low-stress SiN_x increases the refractive index slightly, which has to be taken into account when designing the devices [35], though the index will be always lower than in the silicon (either crystalline or nanocrystalline) core. Importantly, the speed of sound in amorphous SiN_x layers deposited using LPCVD is quite similar to the value we use in our calculations [36], so mechanical leakage will be extremely suppressed. Once the stack with matched stress is available, the patterning of the waveguides is straightforward by optical or e-beam lithography and dry etching.

One might think that removing the silica substrate would completely solve the problem of mechanical leakage. This could be done by assuming a semi-infinite silicon nitride substrate, on top of which the silicon core is defined. However, this solution is quite unrealistic because it is technologically challenging to build thick (≥ 1 μm) Si_3N_4 layers that do not break due to tensile stress. Another choice might consist of replacing the silica substrate by silicon. However, the optical waves would not be fully confined in the upper silicon core due to the high index of the silicon substrate unless the Si_3N_4 layer was very thick, which would lead to the same fabrication issues as mentioned previously.

VIII. CONCLUSIONS

In summary, we show an approach toward unreleased-cavity and waveguide optomechanics in silicon technology. The presented structure relies on vertical engineering: a thick layer of silicon nitride separates the silicon core from the silica substrate, thus reducing the mechanical leakage into the substrate while enabling lossless photonic guidance in the silicon core. Values of the Brillouin gain around 300 1/W m can be achieved in several configurations for mechanical modes with frequencies above 10 GHz when a mechanical Q factor equal to 10^3 is considered, which is usually the case in room-temperature optomechanics in silicon. Much higher values of the Brillouin gain are attainable assuming operation at low temperature, because of the decrease of the acoustic material losses and the subsequent increase of the mechanical Q factor. Indeed, our approach is highly appropriate for quantum optomechanics at cryogenic temperatures since, besides obtaining very large mechanical factors, the intermediate layer provides a path for heat dissipation. Optomechanical structures based on this multilayer system could be fabricated using standard silicon technology. Our findings could pave the way toward unreleased silicon optomechanical circuits, which would overcome the limitations arising from the need to release the silicon core in standard optomechanical circuitry. Moreover, the concept of vertical engineering can be extended to other high-index optomechanical technologies as long as an adequate material for the intermediate layer is employed. We envisage that this unreleased approach may be particularly suitable for application in harsh environments, for example, to employ ultracompact optomechanical microwave oscillators [37] in satellites and spacecraft [38].

ACKNOWLEDGMENTS

This work was supported by the European Commission (PHENOMEN Grant No. H2020-EU-713450), the Universitat Politècnica de València (Grant No. PAID-01-169), the Ministerio de Ciencia, Innovación y Universidades (Grants No. PGC2018-094490-B and No. PRX18/00126), and the Generalitat Valenciana (Grant No. PROMETEO/2019/123).

[1] L. Brillouin, Diffusion de la lumière et des rayons x par un corps transparent homogène, Ann. Phys. **9**, 88 (1922).

[2] R. Y. Chiao, C. H. Townes, and B. P. Stoicheff, Stimulated Brillouin Scattering and Coherent Generation of Intense Hypersonic Waves, Phys. Rev. Lett. **12**, 592 (1964).

[3] E. P. Ippen and R. H. Stolen, Stimulated Brillouin scattering in optical fibers, Appl. Phys. Lett. **21**, 539 (1972).

[4] J. Capmany and D. Novak, Microwave photonics combines two worlds, Nat. Photonics **1**, 319 (2007).

[5] B. Vidal, M. A. Piqueras, and J. Martí, Tunable and reconfigurable photonic microwave filter based on stimulated Brillouin scattering, Opt. Lett. **32**, 23 (2007).

[6] Z. Zhu, D. J. Gauthier, and R. W. Boyd, Stored light in an optical fiber via stimulated Brillouin scattering, Science **318**, 1748 (2007).

[7] B. J. Eggleton, C. G. Poulton, P. T. Rakich, M. J. Steel, and G. Bahl, Brillouin integrated photonics, Nat. Photonics **13**, 664 (2019).

[8] R. Pant, C. G. Poulton, D.-Y. Choi, H. Mcfarlane, S. Hile, E. Li, L. Thevenaz, B. Luther-Davies, S. J. Madden, and B. J. Eggleton, On-chip stimulated Brillouin scattering, Opt. Express **19**, 8285 (2011).

[9] Y. Pennec, V. Laude, N. Papanikolaou, B. Djafari-Rouhani, M. Oudich, S. E. Jallal, J. C. Beugnot, J. M. Escalante, and A. Martínez, Modeling light-sound interaction in nanoscale cavities and waveguides, Nanophotonics **3**, 413 (2014).

[10] A. Choudhary, B. Morrison, I. Aryanfar, S. Shahnia, M. Pagani, Y. Liu, K. Vu, S. Madden, D. Marpaung, and B. J. Eggleton, Advanced integrated microwave signal processing with giant on-chip Brillouin gain, J. Lightwave Technol. **35**, 846 (2017).

[11] D. Marpaung, B. Morrison, M. Pagani, R. Pant, D.-Y. Choi, B. Luther-Davies, S. J. Madden, and B. J. Eggleton, Low-power, chip-based stimulated Brillouin scattering microwave photonic filter with ultrahigh selectivity, Optica **2**, 76 (2015).

[12] A. H. Safavi-Naeini, D. V. Thourhout, R. Baets, and R. V. Laer, Controlling phonons and photons at the wavelength scale: Integrated photonics meets integrated phononics, Optica **6**, 213 (2019).

[13] H. Shin, W. Qiu, R. Jarecki, J. A. Cox, R. H. Olsson, A. Starbuck, Z. Wang, and P. T. Rakich, Tailorable stimulated Brillouin scattering in nanoscale silicon waveguides, Nat. Commun. **4**, 1944 (2013).

[14] R. Van Laer, B. Kuyken, D. Van Thourhout, and R. Baets, Interaction between light and highly confined hypersound in a silicon photonic nanowire, Nat. Photonics **9**, 199 (2015).

[15] R. V. Laer, A. Bazin, B. Kuyken, R. Baets, and D. V. Thourhout, Net on-chip Brillouin gain based on suspended silicon nanowires, New. J. Phys. **17**, 115005 (2015).

[16] J. Chan, A. H. Safavi-Naeini, J. T. Hill, S. Meenehan, and O. Painter, Optimized optomechanical crystal cavity with acoustic radiation shield, Appl. Phys. Lett. **101**, 081115 (2012).

[17] N. T. Otterstrom, R. O. Behunin, E. A. Kittlaus, Z. Wang, and P. T. Rakich, A silicon Brillouin laser, Science **360**, 1113 (2018).

[18] C. J. Sarabalis, J. T. Hill, and A. H. Safavi-Naeini, Guided acoustic and optical waves in silicon-on-insulator for Brillouin scattering and optomechanics, APL Photonics **1**, 071301 (2016).

[19] S. Gundavarapu, G. M. Brodnik, M. Puckett, T. Huffman, D. Bose, R. Behunin, J. Wu, T. Qiu, C. Pinho, N. Chauhan, J. Nohava, P. T. Rakich, K. D. Nelson, M. Salit, and D. J. Blumenthal, Sub-hertz fundamental linewidth photonic integrated Brillouin laser, Nat. Photonics **13**, 60 (2019).

[20] F. Gyger, J. Liu, F. Yang, J. He, A. S. Raja, R. N. Wang, S. A. Bhave, T. J. Kippenberg, and L. Thévenaz, Observation of Stimulated Brillouin Scattering in Silicon Nitride Integrated Waveguides, Phys. Rev. Lett. **124**, 013902 (2020).

[21] C. Wolff, R. Soref, C. Poulton, and B. Eggleton, Germanium as a material for stimulated Brillouin scattering in the mid-infrared, Opt. Express **22**, 30735 (2014).

[22] Y. Liu, N. Dostart, and M. A. Popovi'c, Toward microphononic circuits on chip: An evaluation of components based on high-contrast evanescent confinement of acoustic waves, arXiv:1707.06280 (2017).

[23] W. Qiu, P. T. Rakich, H. Shin, H. Dong, M. Soljačić, and Z. Wang, Stimulated Brillouin scattering in nanoscale silicon step-index waveguides: A general framework of selection rules and calculating SBS gain, Opt. Express **21**, 31402 (2013).

[24] S. R. Mirnaziry, C. Wolff, M. J. Steel, B. J. Eggleton, and C. G. Poulton, Stimulated Brillouin scattering in silicon/chalcogenide slot waveguides, Opt. Express **24**, 4786 (2016).

[25] B. A. Auld, *Acoustic Fields and Waves in Solids* (Wiley, New York, 1973).

[26] C. J. Sarabalis, Y. D. Dahmani, R. N. Patel, J. T. Hill, and A. H. Safavi-Naeini, Release-free silicon-on-insulator cavity optomechanics, Optica **4**, 1147 (2017).

[27] R. Vogelgesang, M. Grimsditch, and J. S. Wallace, The elastic constants of single crystal β-Si_3N_4, Appl. Phys. Lett. **76**, 982 (2000).

[28] W. Jin, R. G. Polcawich, P. A. Morton, and J. E. Bowers, Piezoelectrically tuned silicon nitride ring resonator, Opt. Express **26**, 3174 (2018).

[29] See the Supplemental Material at http://link.aps.org/supplemental/10.1103/PhysRevApplied.15.034021 for more details of the mechanical simulations, including the effect of the area of the substrate considered in the calculations.

[30] G. S. MacCabe, H. Ren, J. Luo, J. D. Cohen, H. Zhou, A. Sipahigil, M. Mirhosseini, and O. Painter, Nano-acoustic resonator with ultralong phonon lifetime, Science **370**, 840 (2020).

[31] V. Laude and J.-C. Beugnot, Generation of phonons from electrostriction in small-core optical waveguides, AIP Adv. **3**, 042109 (2013).

[32] Q. Fan, C. Chai, Q. Wei, P. Zhou, and Y. Yang, Elastic anisotropy and electronic properties of Si_3N_4 under pressures, AIP Adv. **6**, 085207 (2016).

[33] D. Navarro-Urrios, N. E. Capuj, J. Maire, M. Colombano, J. Jaramillo-Fernandez, E. Chavez-Angel, L. L. Martin, L. Mercadé, A. Griol, A. Martínez, C. M. Sotomayor-Torres, and J. Ahopelto, Nanocrystalline silicon optomechanical cavities, Opt. Express **26**, 9829 (2018).

[34] D. Navarro-Urrios, M. F. Colombano, J. Maire, E. Chávez-Ángel, G. Arregui, N. E. Capuj, A. Devos, A. Griol, L. Bellieres, A. Martínez, K. Grigoras, T. Häkkinen, J. Saarilahti, T. Makkonen, C. M. Sotomayor-Torres, and J. Ahopelto, Properties of nanocrystalline silicon probed by optomechanics, Nanophotonics **9**, 4819 (2020).

[35] T. Makino, Composition and structure control by source gas ratio in LPCVD SiN_x, J. Electrochem. Soc. **130**, 450 (1983).

[36] N. Tambo, Y. Liao, C. Zhou, E. M. Ashley, K. Takahashi, P. F. Nealey, Y. Naito, and J. Shiomi, Ultimate suppression of thermal transport in amorphous silicon nitride by phononic nanostructure, Sci. Adv. **6**, eabc0075 (2020).

[37] L. Mercadé, L. L. Martín, A. Griol, D. Navarro-Urrios, and A. Martínez, Microwave oscillator and frequency comb in a silicon optomechanical cavity with a full phononic bandgap, Nanophotonics **9**, 3535 (2020).

[38] M. Metcalfe, Applications of cavity optomechanics, Appl. Phys. Rev. **1**, 031105 (2014).